



Dynamics of double subduction: Numerical modeling

Yury A. Mishin*, Taras V. Gerya, Jean-Pierre Burg, James A.D. Connolly

Department of Earth Sciences, Swiss Federal Institute of Technology Zurich (ETH Zurich), CH-8092 Zurich, Switzerland

ARTICLE INFO

Article history:

Received 31 October 2007

Received in revised form 7 May 2008

Accepted 13 June 2008

Keywords:

Double subduction
Numerical modeling
Mantle tomography
660-km discontinuity
Subducted slab dynamics

ABSTRACT

Double subduction is a geodynamic process in which two plates following each other are synchronously subducted. Double subductions are known for both modern (Izu-Bonin-Marianas and Ryukyu arcs) and ancient (West Himalaya collision zone) plate tectonics. However, our knowledge about this process is limited to conceptual schemes and some restricted analogue experiments. In order to fill this gap we performed 2D numerical experiments using a coupled petrological–thermomechanical approach based on finite differences and marker-in-cell techniques combined with thermodynamic database for the mantle. We investigated the influence of convergence rate, intermediate plate length, activation volume of the mantle dislocation creep and age of the lithosphere. Based on these experiments we conclude that: (A) Subduction rates at two zones running in parallel differ and vary in time even when the total convergence rate remains constant. Supremacy of either subduction zone depends on physical parameters such as (i) relative rates of the plates, (ii) slab ages and (iii) length of the middle plate. (B) Subduction dynamics of the double subduction system involves several processes unknown in simple subduction systems, such as (i) eduction (i.e. “un-subduction”), (ii) subduction re-initiation, (iii) subduction flip triggered by shallow slab breakoff and (iv) turn-over of detached slabs to up-side-down attitudes. (C) Simulated tomographic structures related to slab propagation account for both penetration and non-penetration of the 660 km discontinuity. Non-penetration is favored by (i) low convergence rate, (ii) faster relative movement of the overriding plate, (iii) young age of the subducting slab and (iv) up-side-down turn-over of detached slab.

© 2008 Elsevier B.V. All rights reserved.

1. Introduction

Terrestrial plate tectonics is a complex dynamic system in which several plates are interacting with each other and with the global mantle convection pattern (e.g. Turcotte and Schubert, 2002; Tackley, 2000). Subduction is one of most important features of such interactions and occurs at various types of convergent plate boundaries including intraoceanic settings, active continental margins and continental collision zones. Despite the fact plate dynamics should strongly influence the behaviour of individual subduction zones, subduction processes are predominantly studied using relatively simple two plates (subducting plate + overriding plate) models (e.g. King, 2001). One obvious system that deviates from this simplicity is double subduction—an intriguing process in which two plates following each other are synchronously subducted. Double subduction episodes are characteristic for both modern and ancient plate tectonics and are, in particular, involved into the history of the Himalayan collision zone (e.g. Burg, 2006; Burg et al., 2006), and that of SE Asia leading to the formation of

the active Izu-Bonin-Marianas and Ryukyu arcs (e.g. Hall, 1997). Our knowledge of this process is limited to conceptual schemes (e.g. Burg, 2006) and some restricted analogue experiments (Boutelier et al., 2003) so that double subduction remains enigmatic in terms of physical factors controlling its initiation, duration and dynamics.

In this paper we study the dynamics and stability of double subduction systems. For this purpose, we employ a coupled petrological–thermomechanical numerical model based on finite differences and marker-in-cell techniques combined with thermodynamic database valid for both shallow and deep mantle conditions. These models reveal processes unknown for single subduction, thus offering interpretations to enigmatic geodynamic features that might be characteristic of paleo double subductions.

2. Model setup and governing equations

2.1. Initial configuration

We developed a 2D, coupled petrological–thermomechanical numerical model of double subduction (Fig. 1) using capabilities of the I2VIS code (Gerya and Yuen, 2003a). The spatial coordinate frame of the model is 4000 km × 1500 km. The oceanic crust consists of a 3-km layer of basalts and a 5-km layer of gabbroic rocks.

* Corresponding author. Tel.: +41 44 633 3248; fax: +41 44 633 1065.
E-mail address: yury.mishin@erdw.ethz.ch (Y.A. Mishin).

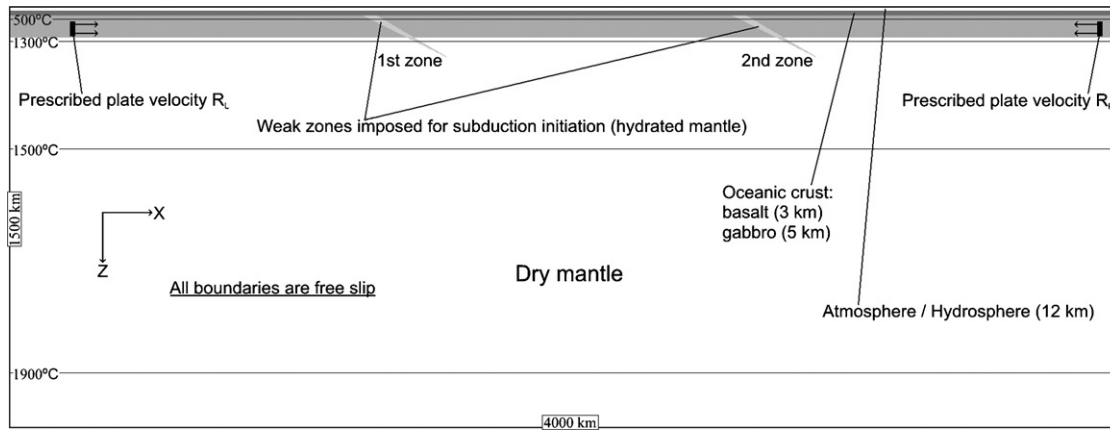


Fig. 1. Numerical model setup.

The top surface of the oceanic crust is calculated dynamically as a free surface by using 12-km thick top layer with low viscosity (10^{18} Pa s) and density (1 kg/m^3 for the atmosphere, 1000 kg/m^3 for the hydrosphere). The interface between this weak layer and the top of the oceanic crust deforms spontaneously and is treated as an erosion/sedimentation surface which evolves according to the transport equation solved at each time step (Gerya and Yuen, 2003b):

$$\frac{\partial z_{es}}{\partial t} = v_z - v_x \frac{\partial z_{es}}{\partial x} - v_s + v_e$$

where z_{es} is a vertical position of the surface as a function of the horizontal distance x ; v_z and v_x are the vertical and horizontal components of material velocity vector at the surface; v_s and v_e are, respectively, gross-scale sedimentation and erosion rates, which correspond to the relation:

$$v_s = 0.0 \text{ mm/yr}, \quad v_e = 0.1 \text{ mm/yr} \quad \text{when } z < 9 \text{ km}$$

$$v_s = 0.1 \text{ mm/yr}, \quad v_e = 0.0 \text{ mm/yr} \quad \text{when } z > 11 \text{ km}$$

The velocity boundary conditions are free slip at all boundaries. Subduction is prescribed by the total convergence rate $R_T = R_R + R_L$, where R_R and R_L are locally imposed constant velocities for the right and the left plates, respectively. Thus the total convergence rate is controlled and not the rates of individual slabs driven by slab-pull. The nucleation of the subduction areas, which are parallel at both sides of the intermediate plate, is imposed by 5–50-km wide weak zones of hydrated mantle cutting across the mantle lithosphere from the bottom of the crust down to 170 km depth with inclination angle 30° . Taking into account the critical role of water for subduction initiation (Regenauer-Lieb et al., 2001) these zones are characterized by wet olivine rheology (Ranalli, 1995) and a low plastic strength limit of 1 MPa. With progressing subduction, these zones are spontaneously substituted by weak upper oceanic crust, which is also characterized by low plastic strength. This device implies high pressure fluids to be present along the slab interface during subduction (e.g. Sobolev and Babeyko, 2005; Gerya et al., 2008).

The initial geotherm for the lithosphere is defined via half-space cooling model (e.g. Turcotte and Schubert, 2002; Fowler, 2005) for the prescribed lithospheric age A . Different values of the age of the lithosphere were used to study the influence of this parameter on the dynamics of double subduction. The geotherm for the mantle below the lithosphere is defined by prescribing nearly adiabatic temperature gradient of 0.5 K/km .

2.2. Petrological model

The stable mineralogy and physical properties for the various lithologies were computed by free energy minimization (Connolly, 2005) as a function of pressure and temperature. The properties of sediments and hydrated mantle are required only at depths of less than 200 km where the properties of hydrated crustal and mantle rocks strongly affect plate interaction and subduction dynamics (e.g. Gerya et al., 2008). This is an argument that the properties are required at less than 200 km, but not that they are not required at greater depth. Accordingly, we employ for these two lithologies the results of previous thermodynamic models (Gerya et al., 2006). However, expanding models to lower mantle depths requires a robust equation of state for the calculation of the properties of the subducted oceanic crust and mantle. For this purpose, we adopted the Mie-Grueneisen formulation of Stixrude and Bukowinski (1990) with the parameterization of Stixrude and Lithgow-Bertelloni (2005) augmented for lower mantle phases as described by Khan et al. (2006). This parameterization limits the chemical model to the $\text{CaO-FeO-MgO-Al}_2\text{O}_3\text{-SiO}_2$ with the phases summarized in Table 1. The mantle is assumed to have a pyrolytic composition, for which the thermodynamic parameterization is adequate to reproduce the expected lower mantle phase relations

Table 1

Phase notation and formulae for the $\text{CaO-FeO-MgO-Al}_2\text{O}_3\text{-SiO}_2$ pyrolytic and basalt models (Fig. 2)

Symbol	Phase	Formula
aki	Akimotoite	$\text{Mg}_x\text{Fe}_{1-x}\text{Al}_2\text{Si}_{1-y}\text{O}_3$, $x + y \leq 1$
an	Plagioclase	$\text{CaAl}_2\text{Si}_2\text{O}_8$
c2/c	Pyroxene	$[\text{Mg}_x\text{Fe}_{1-x}]_4\text{Si}_4\text{O}_{12}$
cpv	Ca-perovskite	CaSiO_3
cpx	Clinopyroxene	$\text{Ca}_2\text{Mg}_{4-2x-2y}\text{Fe}_{2x}\text{Si}_4\text{O}_{12}$
gt	Garnet	$\text{Fe}_3\text{Ca}_3\text{Mg}_3(1-x+y+z/3)\text{Al}_{2-2z}\text{Si}_{3+z}\text{O}_{12}$, $x + y \leq 1$
o	Olivine	$[\text{Mg}_x\text{Fe}_{1-x}]_2\text{SiO}_4$
opx	Orthopyroxene	$[\text{Mg}_x\text{Fe}_{1-x}]_{4-2y}\text{Al}_{4(1-y)}\text{Si}_4\text{O}_{12}$
ppv	Post-perovskite	$\text{Mg}_x\text{Fe}_{1-x}\text{Al}_2\text{Si}_{1-y}\text{O}_3$, $x + y \leq 1$
pv	Perovskite	$\text{Mg}_x\text{Fe}_{1-x}\text{Al}_2\text{Si}_{1-y}\text{O}_3$, $x + y \leq 1$
ring	Ringwoodite	$[\text{Mg}_x\text{Fe}_{1-x}]_2\text{SiO}_4$
sp	Spinel	$\text{Mg}_x\text{Fe}_{1-x}\text{Al}_2\text{O}_3$
stv	Stishovite	SiO_2
wad	Wadsleyite	$[\text{Mg}_x\text{Fe}_{1-x}]_2\text{SiO}_4$
wus	Magnesiowuestite	$\text{Mg}_x\text{Fe}_{1-x}\text{O}$

Thermodynamic data is from Stixrude and Lithgow-Bertelloni (2005) augmented for lower mantle phases as described by Khan et al. (2006). Unless otherwise noted, the compositional variables w , x , y , and z may vary between zero and unity and are determined as a function of pressure and temperature by free-energy minimization (Connolly, 2005).

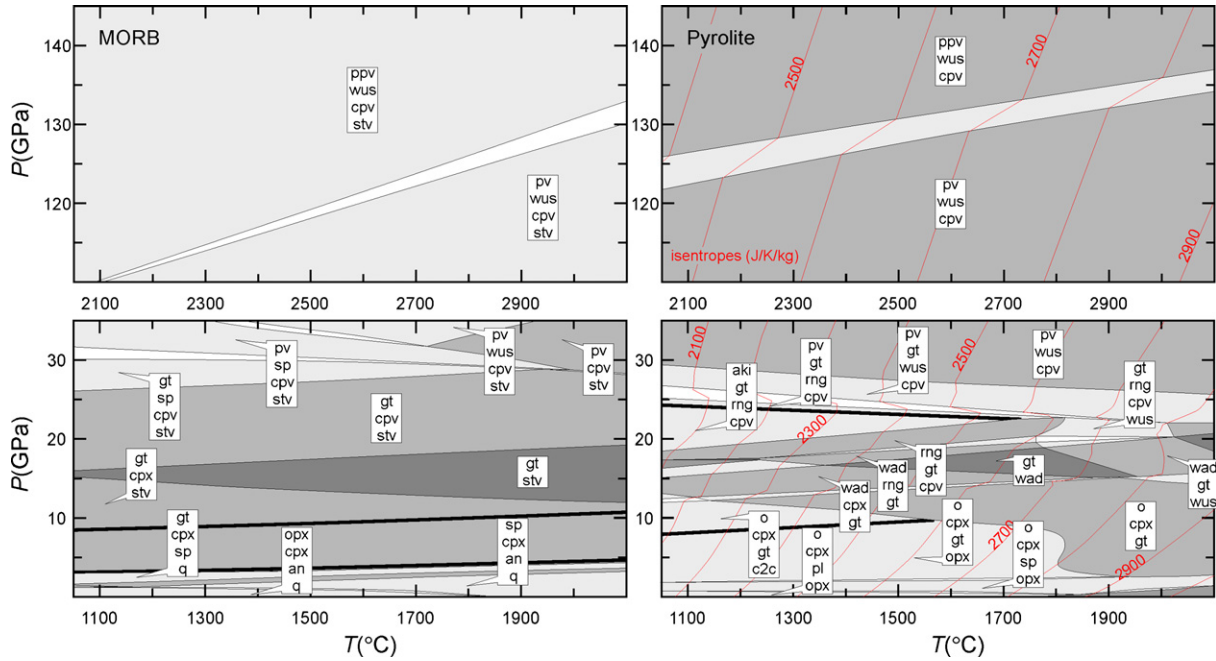


Fig. 2. Phase relations for the CaO–FeO–MgO–Al₂O₃–SiO₂ pyrolite and basalt models (see Table 1 for notation). To permit resolution of phase relations the diagrams are split to exclude the large depth interval between the transition zone and core–mantle boundary in which the models do not predict phase transformations. Compositions for the pyrolite and basalt models are, respectively 3.87 wt% CaO, 8.11 wt% FeO, 3.61 wt% Al₂O₃, 38.59 wt% MgO and 45.82 wt% SiO₂; and 11.86 wt% CaO, 11.25 wt% FeO, 13.72 wt% Al₂O₃, 8.64 wt% MgO and 54.54 wt% SiO₂.

(Fig. 2). Application of the thermodynamic model to the basaltic composition of the oceanic crust is more problematic because phase equilibrium experiments (Hirose and Fei, 2002; Irifune and Ringwood, 1993; Irifune et al., 1994; Ono et al., 2005) suggest the existence of several high pressure phases that are not characterized well enough to be included in our parameterization. Additionally, the CaO–FeO–MgO–Al₂O₃–SiO₂ model excludes volatile oxides, notably K₂O and Na₂O, that are more significant in the subducted oceanic crust, as a consequence our model is likely to overestimate the basalt–pyrolite density contrast ($\rho_{\text{basalt}}/\rho_{\text{pyrolite}}$, Fig. 3). To calibrate this effect, we find that experimentally derived density estimates for K₂O–Na₂O–CaO–FeO–MgO–Al₂O₃–SiO₂ (Irifune

and Ringwood, 1993; Ono et al., 2005) are 1.7–2.3% below those calculated here. Accordingly, neutral buoyancy in the earth's interior most probably corresponds to conditions at which our basalt–pyrolite density contrast is 1.02 ± 0.03 .

2.3. Thermomechanical model

The momentum, continuity, and temperature equations for the two-dimensional creeping flow, accounting for both thermal and chemical buoyancy, are solved using the I2VIS code based on conservative finite differences and non-diffusive marker-in-cell techniques (Gerya and Yuen, 2003a).

The conservation of mass is prescribed by the incompressible continuity equation:

$$\frac{\partial v_x}{\partial x} + \frac{\partial v_z}{\partial z} = 0$$

The 2D Stokes equations for creeping flow take the form:

$$\frac{\partial \sigma_{xx}}{\partial x} + \frac{\partial \sigma_{xz}}{\partial z} = \frac{\partial P}{\partial x}$$

$$\frac{\partial \sigma_{zz}}{\partial z} + \frac{\partial \sigma_{xz}}{\partial x} = \frac{\partial P}{\partial z} - g\rho(T, P, C)$$

The density $\rho(T, P, C)$ depends explicitly on the temperature (T), the pressure (P), and the rock composition (C).

The Lagrangian temperature equation includes latent heat effects of phase transformations in the crust and mantle and is formulated as (Gerya and Yuen, 2003a)

$$\rho C_p \left(\frac{DT}{Dt} \right) = -\frac{\partial q_x}{\partial x} - \frac{\partial q_z}{\partial z} + H_r + H_a + H_s + H_L$$

$$q_x = -k(T, C) \frac{\partial T}{\partial x}, \quad q_z = -k(T, C) \frac{\partial T}{\partial z}$$

$$H_a = T\alpha \frac{DP}{Dt}$$

$$H_s = \sigma_{xx} \dot{\epsilon}_{xx} + \sigma_{zz} \dot{\epsilon}_{zz} + \sigma_{xz} \dot{\epsilon}_{xz}$$

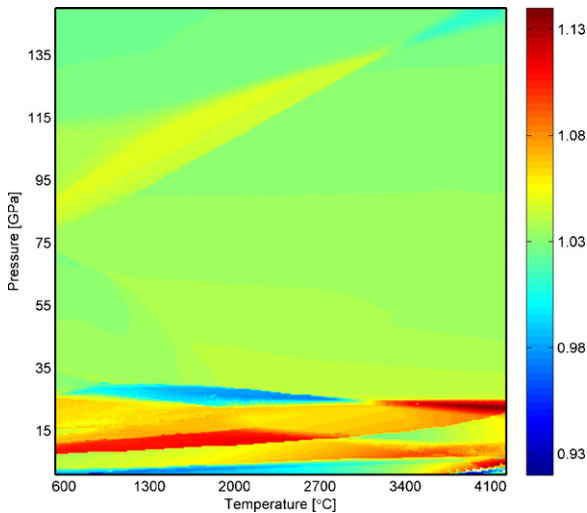


Fig. 3. Density contrast ($\rho_{\text{basalt}}/\rho_{\text{pyrolite}}$, color scale indicated by the color bar to the right) between pyrolite and basalt computed from the thermodynamic model (Fig. 2, Table 1). Except for a pressure interval corresponding to the base of the transition zone, basalt is predicted to be denser than pyrolite, with a typical density contrast of 1–3% in the lower mantle.

where D/Dt is the substantive time derivative; x and z denote the horizontal and vertical coordinates, respectively; $\sigma_{xx}, \sigma_{zz}, \sigma_{xz}$ are the components of the deviatoric stress tensor; $\dot{\epsilon}_{xx}, \dot{\epsilon}_{zz}, \dot{\epsilon}_{xz}$ are the components of the strain rate tensor; P is the pressure; T is the temperature; q_x and q_z are the heat fluxes; ρ is the density; $k(T, C)$ is the thermal conductivity; C_p is the isobaric heat capacity; H_r, H_a, H_s and H_l denote the radiogenic, adiabatic, shear, and latent heat production, respectively. In order to account for physical effects of phase transitions on the dynamics of double subduction we used coupled petrological–thermomechanical numerical modeling approach described in detail by Gerya et al. (2004a, 2006). According to this approach all local rock properties, including effective density, isobaric heat capacity, thermal expansion, adiabatic and latent heating are calculated at every time step based on Gibbs energy minimization.

Viscosity dependent on strain rate, pressure and temperature is defined in terms of deformation invariants (Ranalli, 1995) as

$$\eta_{\text{creep}} = (\dot{\epsilon}_{\text{II}})^{(1-n)/2n} F(A_D)^{-1/n} \exp\left(\frac{E_a + V_a P}{nRT}\right)$$

where $\dot{\epsilon}_{\text{II}} = 1/2 \dot{\epsilon}_{ij} \dot{\epsilon}_{ij}$ is the second invariant of the strain rate tensor and A_D, E_a and n are experimentally determined flow law parameters (Table 2). We use different values of the effective activation volume V_a to study the influence of this parameter on the dynamics of double subduction. F is a dimensionless coefficient depending on the type of experiments on which the flow law is based. For example:

$$F = \frac{2^{(1-n)/n}}{3^{(1+n)/2n}}, \quad \text{for triaxial compression and}$$

$$F = 2^{(1-2n)/n}, \quad \text{for simple shear}$$

The ductile rheology is combined with a brittle rheology to yield an effective viscoplastic rheology. For this purpose the Mohr–Coulomb yield criterion (e.g. Ranalli, 1995) is implemented by limiting creep viscosity, η_{creep} , as follows:

$$\eta_{\text{creep}} \leq \frac{c + P \sin(\varphi)}{(4\dot{\epsilon}_{\text{II}})^{1/2}}$$

where P is dynamic (non-lithostatic) pressure, c is the cohesion (residual strength at $P=0$) and φ is internal friction angle (Table 2). Assuming high pore fluid pressure in hydrated rocks (e.g. Gerya et al., 2008) brittle–plastic strength of upper oceanic crust (basalts, sediments) was taken low (1 MPa) allowing efficient decoupling along the interface of subducting slabs.

3. Results

Sixteen experiments (Table 3) were performed to study the influence of (1) the convergence rate R_T , (2) the intermediate plate length L , (3) the mantle dislocation creep activation volume V_a and (4) the age A of the lithosphere on the dynamics of double subduction.

3.1. Reference model

The reference model was chosen to have the following parameters: total convergence rate $R_T = 7.0$ cm/yr ($R_L = 3.5$ cm/yr, $R_R = -3.5$ cm/yr), intermediate plate length $L = 700$ km, mantle dislocation creep activation volume $V_a = 0.8$ J/bar and age of the lithosphere $A = 30$ Myr (Fig. 4 – initial temperature and viscosity profiles, Figs. 5–7 – results of numerical experiments).

Subduction in the reference model starts almost synchronously at both extremities of the intermediate plate, but the left zone becomes rapidly dominant while the right subduction zone ceases.

Table 2
Material properties used in numerical experiments

Material	Thermal conductivity k , W/(m K)	Flow law	Activation energy E_a (kJ/mol)	Material constant A_D , 1/(MPa ⁿ s)	Stress exponent n	Radiogenic heating H_r ($\times 10^{-6}$ W/m ³)	Cohesion c (MPa)	Friction angle $\sin(\varphi)$
Sedimentary rocks	$0.64 + \frac{807}{T+77}$	Wet quartzite	154	$10^{-3.5}$	2.3	1.50	1.0	0.0
Upper oceanic crust	$1.18 + \frac{474}{T+77}$	Wet quartzite	154	$10^{-3.5}$	2.3	0.25	1.0	0.0
Lower oceanic crust	$1.18 + \frac{474}{T+77}$	Plagioclase (AN ₇₅)	238	$10^{-3.5}$	3.2	0.25	1.0	0.6
Dry mantle	$0.73 + \frac{1293}{T+77}$	Dry olivine	532	$10^{4.4}$	3.5	0.022	1.0	0.6
Hydrated mantle	$0.73 + \frac{1293}{T+77}$	Wet olivine	470	$10^{3.3}$	4.0	0.022	1.0	0.0
References ^a	1	2	2	2	2	3	4	4

^a 1, Clauser and Huenges (1995); 2, Ranalli (1995); 3, Turcotte and Schubert (2002); 4, Gerya et al. (2008).

Table 3
Description of the numerical experiments used in this work

Run	Prescribed plate velocities R_L/R_R (cm/yr)	Length of the middle plate L (km)	Dislocation creep activation volume V_a (J/bar)	Lithospheric age A (Myr)
Model 1 (Reference)	3.5/–3.5	700	0.8	30
Model 2	1.0/–1.0	700	0.8	30
Model 3	7.0/0.0	700	0.8	30
Model 4	0.0/–7.0	700	0.8	30
Model 5	7.0/–7.0	700	0.8	30
Model 6	3.5/–3.5	500	0.8	30
Model 7	3.5/–3.5	900	0.8	30
Model 8	3.5/–3.5	1100	0.8	30
Model 9	3.5/–3.5	1300	0.8	30
Model 10	3.5/–3.5	700	0.6	30
Model 11	3.5/–3.5	700	1.0	30
Model 12	3.5/–3.5	700	1.2	30
Model 13	3.5/–3.5	700	0.8	10
Model 14	3.5/–3.5	700	0.8	50
Model 15	3.5/–3.5	700	0.8	70
Model 16	3.5/–3.5	700	0.8	100

Accelerated subduction of the left plate leads the corresponding slab to deflect downward and pierce the 660 km discontinuity (as is the case for the Tonga slab Roth and Wiens, 1999) and the Mariana slab (Tibi et al., 2006) and, later, the slab to breakoff at shallow depth. Breakoff results in opening a new spreading centre behind the floundering slab that sinks into the deep mantle. In our model slab detachment occurs during ongoing subduction which is different from the previous thermomechanical studies of slab breakoff (Gerya et al., 2004b; Andrews and Billen, in press) modeled dynamics of this process after ceasing of active subduction and obtained depths of detachment varying from 100 to 300 km. Shallow detachment of the slab in our models is caused by viscoplastic necking process triggered by strong extensional forces imposed on the horizontal segment of the plate by rapidly subducting and retreating cold and dense slab. The gap formed by shallow slab detachment is filled by hot asthenospheric mantle rapidly rising to the surface

and building new young (1–1.5 Myr) and thin oceanic lithosphere (Fig. 5, 23.2–24.6 Myr).

3.2. Influence of convergence rate

Subduction rate and length along both zones are strongly dependent on the ratio between imposed plate velocities R_L and R_R (Fig. 8). Keeping the same total convergence rate R_T but with different plate velocities, either the left zone (when $R_L > R_R$, Fig. 8b) or the right one (when $R_L < R_R$, Fig. 8c) dominates the system. In the latter case, the middle plate is wholly subducted and comes to rest up-side-down on the 660 km discontinuity (Fig. 8c, 6.6 Myr), a geometry that provides an interpretation of “stagnant” slabs as imaged below the Northwest Pacific (e.g. Tajima and Grand, 1998). When $R_L = R_R$, subduction starts at both zones simultaneously, but the left zone becomes dominant

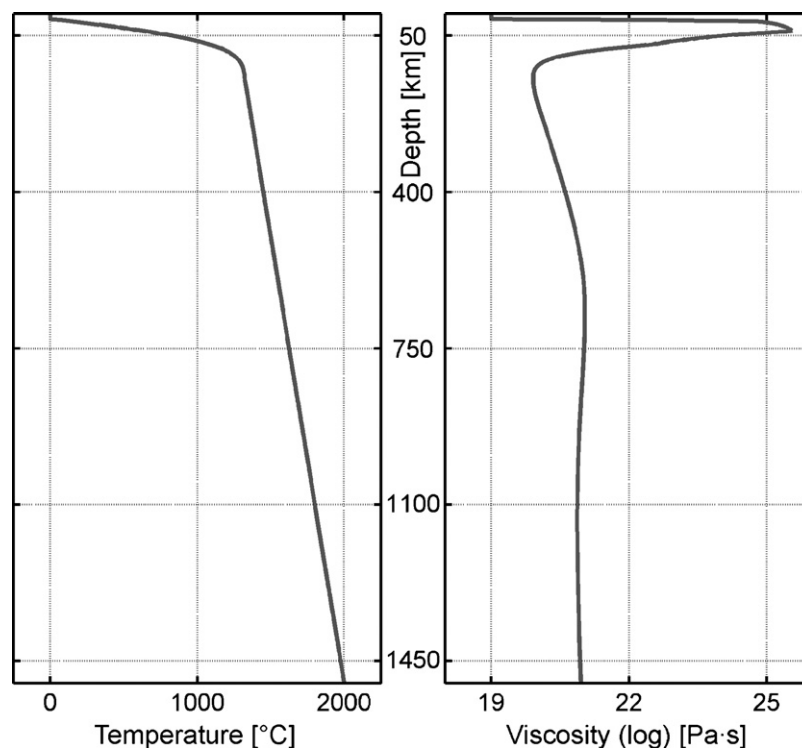


Fig. 4. Initial temperature and viscosity profiles for the reference Model 1 (Table 3).

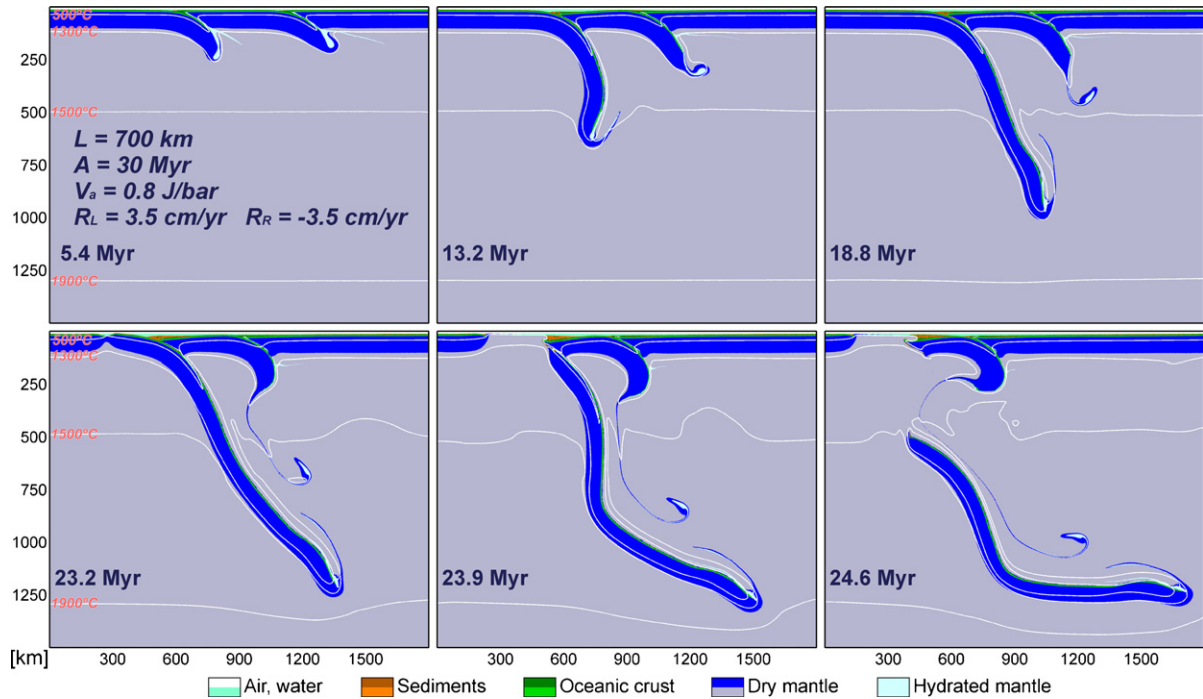


Fig. 5. Evolution of lithological field in the reference Model 1 (Table 3).

as convergence proceeds and even notable *eduction* (i.e. “un-subduction”—return to the surface of deeply buried slab, in the sense of Andersen et al., 1991) of the previously subducted right slab can take place, especially at relatively low total convergence rate (Fig. 8a).

Decrease of the total convergence rate causes slow subduction and the left plate can interact with, but does not penetrate into the

660 km discontinuity, something reminiscent of the slab beneath the central Izu-Bonin arc (Takenaka et al., 1999). This situation also occurs when R_L is larger than R_R .

The dynamics does not change significantly for convergence rates larger than in the reference case, but the process develops more rapidly and subduction entrains coupled slabs (Fig. 8d), as it may be the case in Japan, beneath Tokyo (Wu et al., 2007).

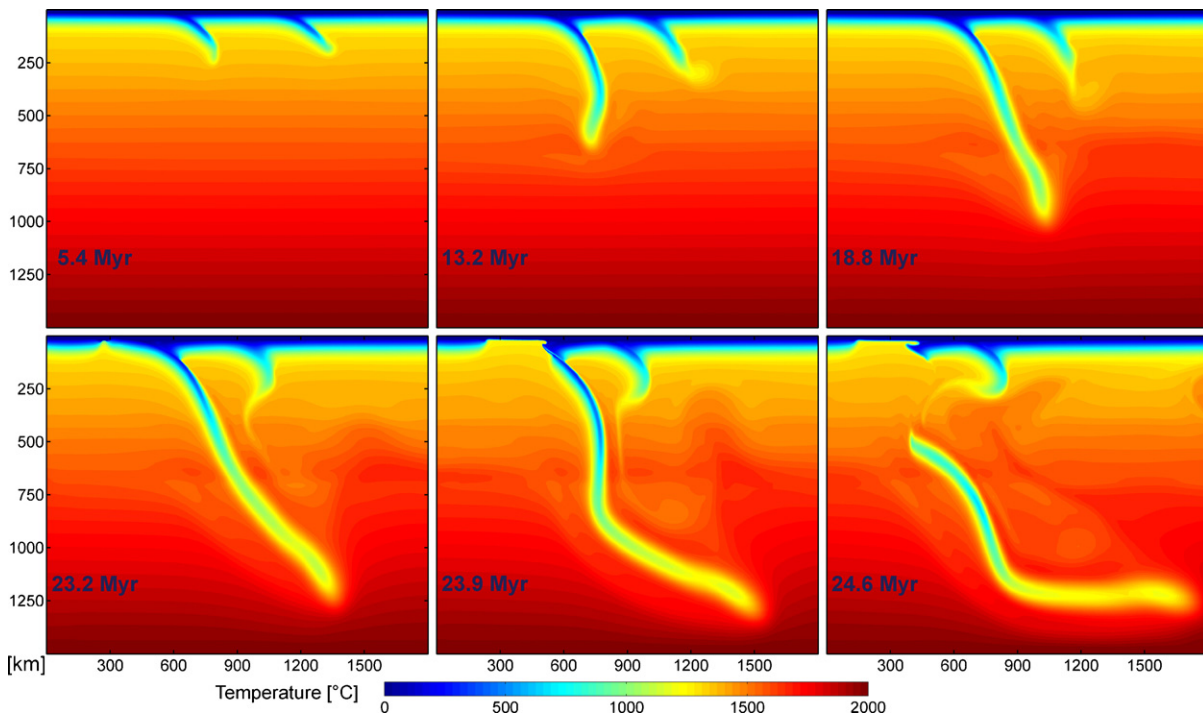


Fig. 6. Evolution of temperature field in the reference Model 1 (Table 3).

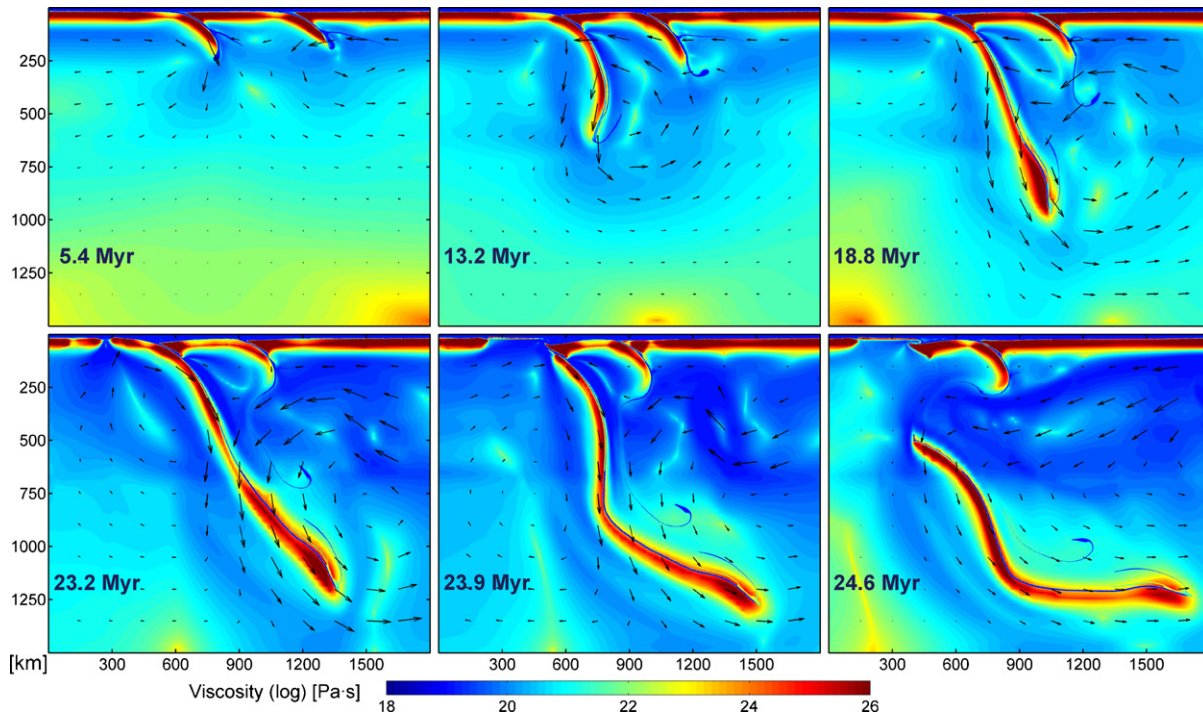


Fig. 7. Evolution of viscosity and velocity fields in the reference Model 1 (Table 3).

3.3. Influence of the intermediate plate length

Depending on the length L of the intermediate plate (i.e. inter-subduction space) two fundamental regimes have been obtained (Fig. 9):

- (1) Models with a relatively short (500–900 km) middle plate are characterized by evident dominance of the left subduction zone (Figs. 5 and 9a and b) with high probability of eduction at the right plate boundary (e.g. Fig. 9a). Normally shallow breakoff (viscoplastic necking) of the left slab at depths less than 100 km causes the formation of a new spreading centre (Fig. 5, 23.2–23.9 Myr, Fig. 9a and b). The sinking slab can initiate subduction of the middle plate in the direction opposite to the original one (subduction flip, and the plate can be even turned over because of slab coupling (Fig. 9b, 24.8–25.7 Myr)). Such a relationship between breakoff and flip has been envisioned for Taiwan (Teng et al., 2000).
- (2) As the length of the plate is increased to 1100–1300 km, a notable change in the system dynamics occurs (Fig. 9c and d). At these conditions the right zone becomes active and subduction intensity along both zones becomes almost balanced. The right zone may even predominate at some time intervals (Fig. 9c, 17 Myr). In such a system, the middle plate is wholly subducted and rotates to an up-side-down position in the lower mantle (Fig. 9c, 18.1–18.7 Myr, Fig. 9d, 17.1–18.4 Myr).

Interaction of the subducting slabs with the 660 km discontinuity does not apparently depend on the length of the intermediate plate since in all models designed to test this geometrical configuration all slabs break through the 660 km discontinuity (Figs. 5 and 9).

3.4. Influence of mantle rheology

All numerical experiments performed to study the influence of mantle dislocation creep activation volume V_a show supremacy

of the left subduction, but this predominance decreases with increasing activation volume and thus with growing viscous resistance of the asthenospheric mantle at large depth (Fig. 10). Even for relatively small activation volume of 0.6 J/bar, rapid eduction of the right zone may take place (Fig. 10a, 9.4–10.3 Myr). At noticeably higher $V_a = 1.0$ –1.2 J/bar, eduction does not occur and subduction rates in the two zones become almost balanced (Fig. 10b and c).

At smaller activation volume the left plate rapidly sinks into the mantle and penetrates the 660 km discontinuity before breaking off at shallow depths of 0–100 km (Fig. 10a, 10.3–10.5 Myr). With increase of the activation volume, the right subduction zone becomes active and the two slabs become coupled (Fig. 10b and c). The coupled slabs can either sink into the lower mantle ($V_a = 1.0$ J/bar, Fig. 10b) or (at largest tested value $V_a = 1.2$ J/bar, Fig. 10c) can be flattened and deferred at the 660 km discontinuity.

3.5. Influence of age of the lithosphere

Numerical experiments show that for a wide range of lithospheric age ($A = 10$ –70 Myr) the left zone dominates with almost no activity on the right one (Figs. 5 and 11a–c). However, with an old and strong lithosphere ($A = 100$ Myr) the left zone may become inactive and (at least at the beginning of convergence) the right zone dominates (Fig. 11d). In that case the middle plate is completely subducted and may rotate to an up-side-down position (Fig. 11d, 10.2–19.4 Myr). And because of inactivity of the left plate two weak zones can even merge.

With a younger plate ($A = 10$ –70 Myr), the left slab quickly sinks into the mantle, but its interaction with the 660 km discontinuity varies depending on the slab age. Young ($A < 30$ Myr) and weak slabs are deferred by the discontinuity and flatten (Fig. 11a). With increased A , subducting slabs become stronger and denser and penetrate the 660 km discontinuity (Figs. 5 and 11b and c). Shallow breakoff of these slabs occurs for intermediate slab

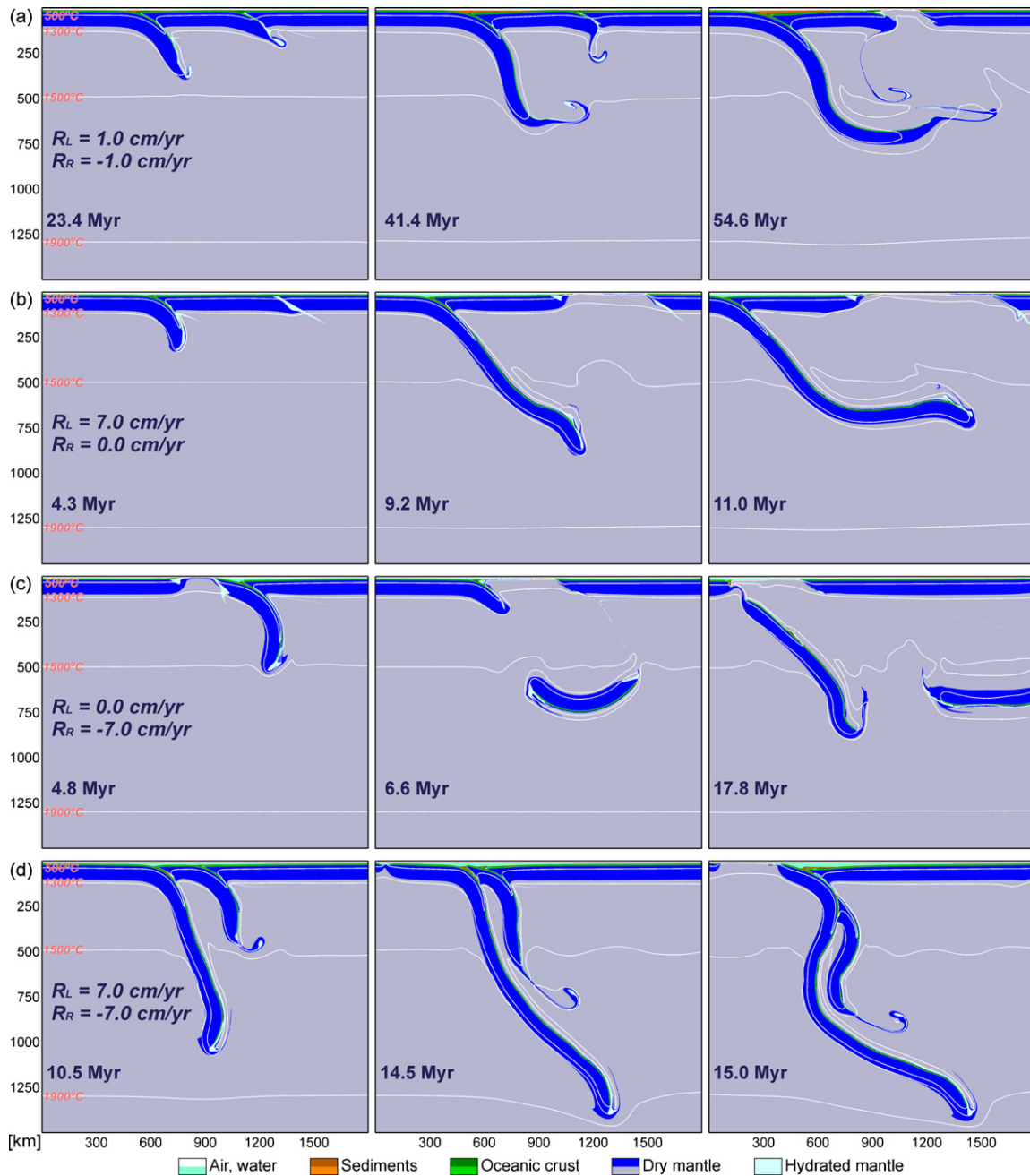


Fig. 8. Influence of convergence rate on the dynamics of double subduction. (a) Model 2, (b) Model 3, (c) Model 4 and (d) Model 5 (model descriptions in Table 3).

ages of 30–50 Myr (Fig. 5, 23.2–23.9 Myr, Fig. 11b, 20.7–21.1 Myr). Penetration of the 660 km discontinuity normally results in education process at the right zone (Fig. 11b, 18.4–20.7 Myr, Fig. 11c, 22.3–24.4 Myr), and if the educated middle plate is sufficiently old and dense, subduction of this plate can spontaneously restart (Fig. 11c, 25.3 Myr).

4. Discussion and implications

4.1. Paired subduction dynamics

Paired subduction systems on the active earth offer a limited number of patterns: i.e. divergent subduction as the Molucca Sea between the Halmahera and Sangihe island arcs (e.g. Hall et al.,

1995) and on both sides of the Adriatic sea (e.g. Doglioni et al., 2007), confronting subduction like the Manila and Philippine-Ryukyu trenches on both sides of the Philippine Islands and parallel subduction like the Pacific Plate and the Philippine Sea along the Izu-Bonin and Nankai-Ryukyu trenches, respectively (Hall et al., 1995). Such patterns locally lead to complex interference between overlapping slabs (Ishida, 1992; Wu et al., 2007). Yet, these examples determine the relevance of the presented models. Numerical experiments show that subduction along two parallel and synchronous zones is typically unbalanced: subduction rates at both zones are irregular over time (Fig. 12). One may expect that such irregular motions are associated in 3D with plate rotations, as the Philippine Plate did (Hall et al., 1995). Though in most cases the left subduction zone dominates

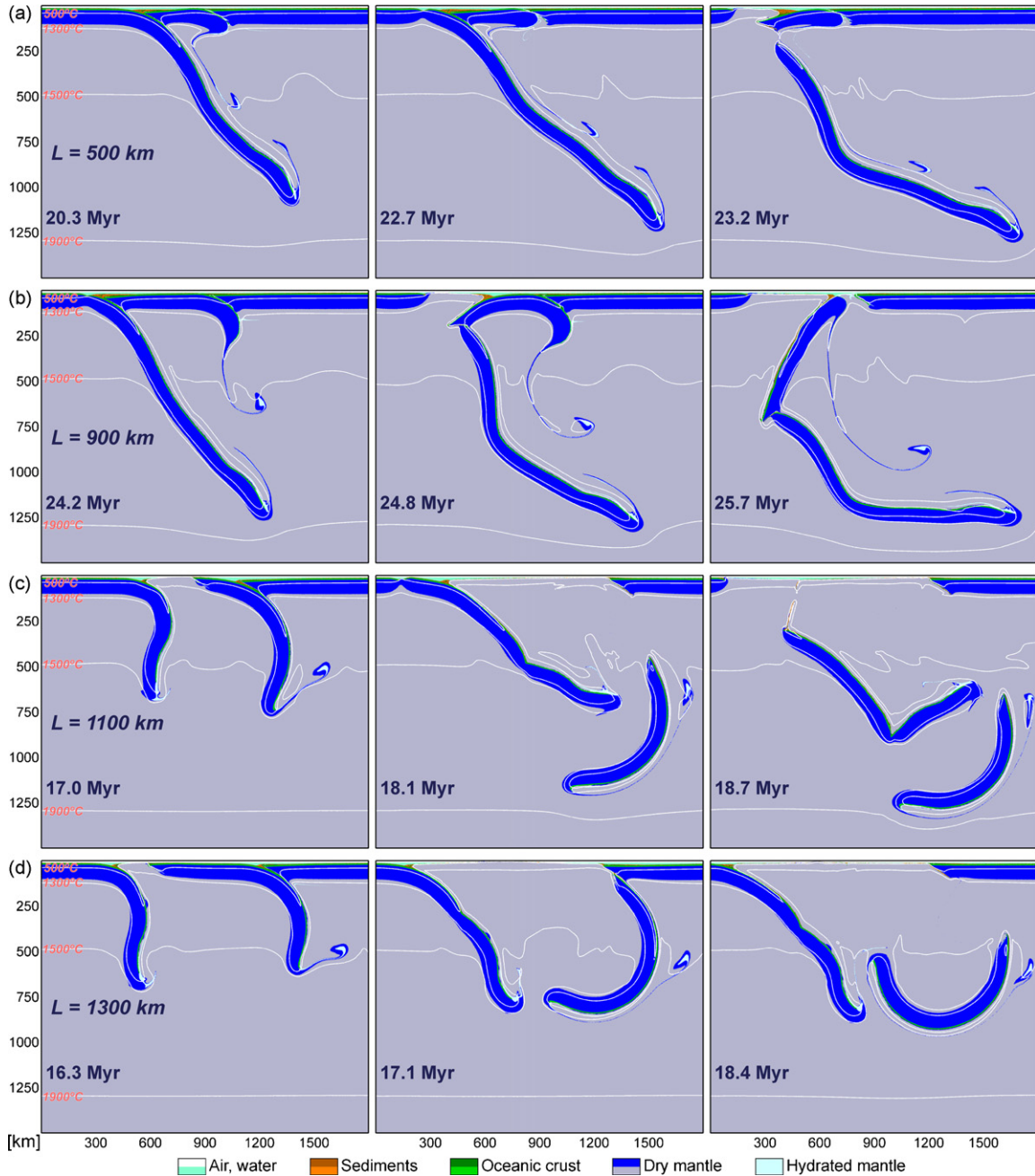


Fig. 9. Influence of length of the intermediate plate on the dynamics of double subduction. (a) Model 6, (b) Model 7, (c) Model 8 and (d) Model 9 (model descriptions in Table 3).

(e.g. Figs. 5, 8a, b and d, 9a and b, 10a, 11a–c, and 12a and b), a range of physical conditions (e.g. longer middle plate, Figs. 9c and d and 12c and d, dominating convergence from the right plate, Fig. 8c, old age of the lithosphere, Fig. 11d) lead subduction at the right zone to dominate. Strong subduction rate variations at constant total convergence rate (Fig. 12) imply large variations in magmatic production on either coeval arc. Such variations may explain the clustered age distribution of calc-alkaline magmatism on both sides of the Karakoram-Kohistan Suture Zone in Pakistan (e.g. Treloar et al., 1996).

Plots Fig. 12c and d illustrate almost balanced subduction rates along the two zones at the beginning, with later alternation of their

activities, the right zone becoming more active than the left one. This behaviour is characteristic for relatively long (1100–1300 km) middle plates (Fig. 9c and d).

Explanation for subduction velocity behaviour is related to the variable degree of coupling along two parallel and synchronous subduction zones. When $R_L = R_R$, subduction starts at both zones simultaneously, but the left zone is dominated by movement of the subducting plate while the right one by movement of the overriding plate. As demonstrated by van Hunen et al. (2000) and Manea and Gurnis (2007) the movement of an overriding plate tends to produce shallower subduction and stronger plate coupling than the movement of a subducting plate. Therefore the subduction in the right zone causes more resistance to the plate

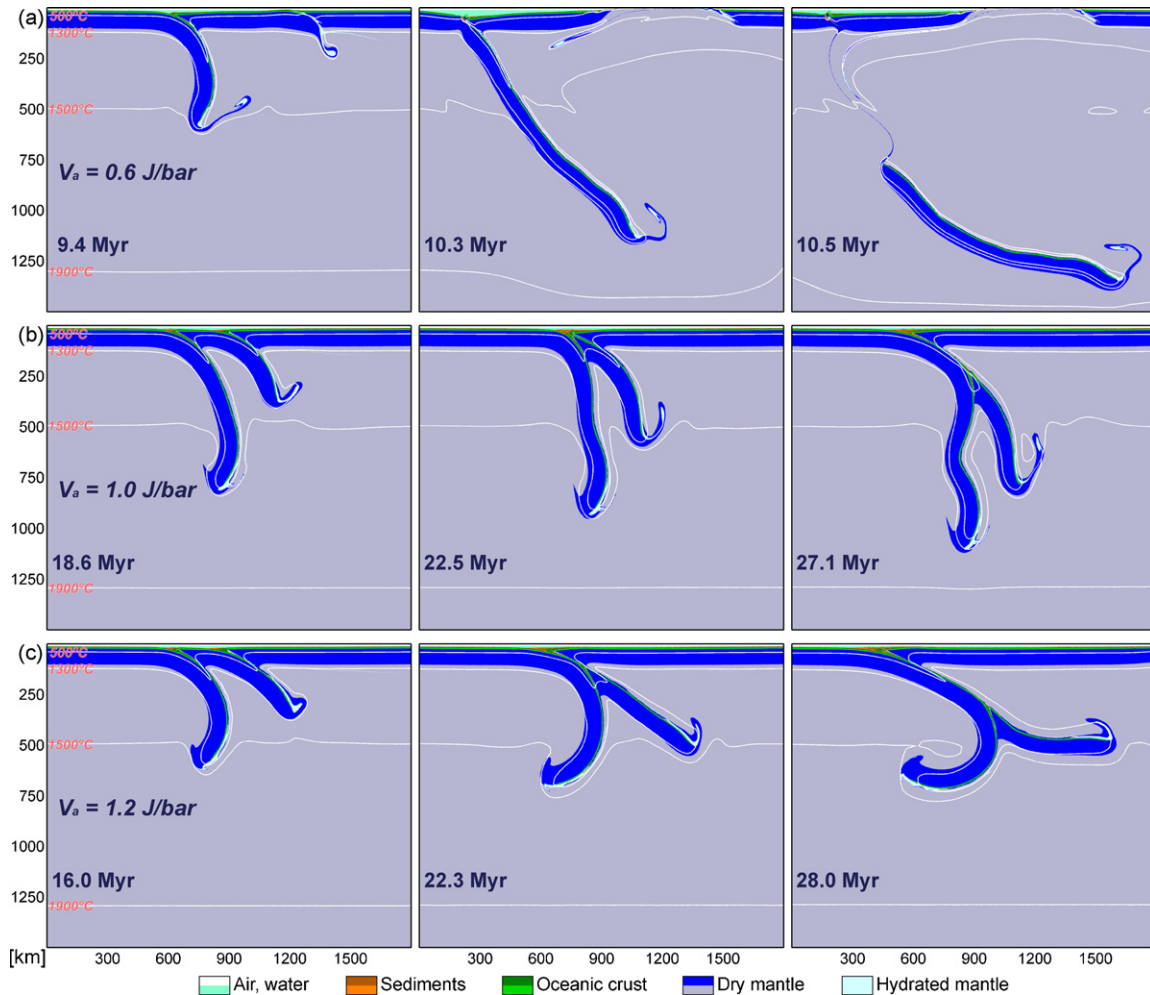


Fig. 10. Influence of mantle rheology on the dynamics of double subduction. (a) Model 10, (b) Model 11 and (c) Model 12 (model descriptions in Table 3).

movement then the subduction in the left zone and tends to decelerate (Fig. 12a and b). Also bending of the middle plate in the right zone exerts tendency of lifting up its opposite edge above the left zone which additionally decreases resistance to subduction in the left zone. This lifting tendency is maximal for short plates and therefore these plates show stronger dominance of the left zone (cf. Fig. 12a, b and c, d).

Models of the double subduction systems involve processes yet unrecognized for simple subduction systems. Those are in particular eduction and subduction alternance, with cessation and reactivation of subduction zones and subduction flip. Several models involve eduction, almost always associated with subduction rate variations (Fig. 12a). As it can be seen from the plot, the dynamics of such a system is characterized by rapid acceleration of the left plate until shallow breakoff, and rapid deceleration and ultimate eduction of the middle plate (negative subduction rate at the second zone on the plot). Yet rate variations do not necessarily lead to eduction (Fig. 12b). As in the previous case (Fig. 12a), the left zone clearly dominates and finally the slab can breakoff at shallow depth (e.g. Model 1 in Table 3, Fig. 5), but eduction does not occur in such a system. Though subduction rate at the second zone decreases with time and can be even zero (as subduction at the second zone can cease, e.g. Model 1 in Table 3, Fig. 5), it is never negative.

4.2. Specific cases

Rapid sinking of the left plate results in subduction hinge retreat and back-arc extension in the overriding plate. In double subduction systems, slab rollback causes eduction of the middle plate, and a new spreading centre can form between the middle and right plates. Eduction can be relevant to the origin of some blueschist complexes. As discussed by Maresch and Gerya (2005) blueschist complexes in several places in the world (e.g. in Caribbean) are formed in evolving, nascent intraoceanic subduction zones without obvious coeval volcanism, raising the question of the minimum subduction duration, amount of convergence, and exhumation mechanisms necessary to produce them. Eduction is a mechanism for the rapid formation and exhumation of such complexes.

When the intermediate plate is old and dense, the second subduction can restart (Fig. 13, 25.7 Myr). This is due to the gravitational instability driven by a strong density contrast between the cold retreating middle plate and the hot asthenospheric mantle rising into the forming spreading center. Similar mechanism of subduction initiation by gravitational instability across a zone (transform fault) separating two plates with contrasting thermal structures is suggested by Hall et al. (2003). We suggest that this mechanism can have broader significance in case of eduction and multiple plate

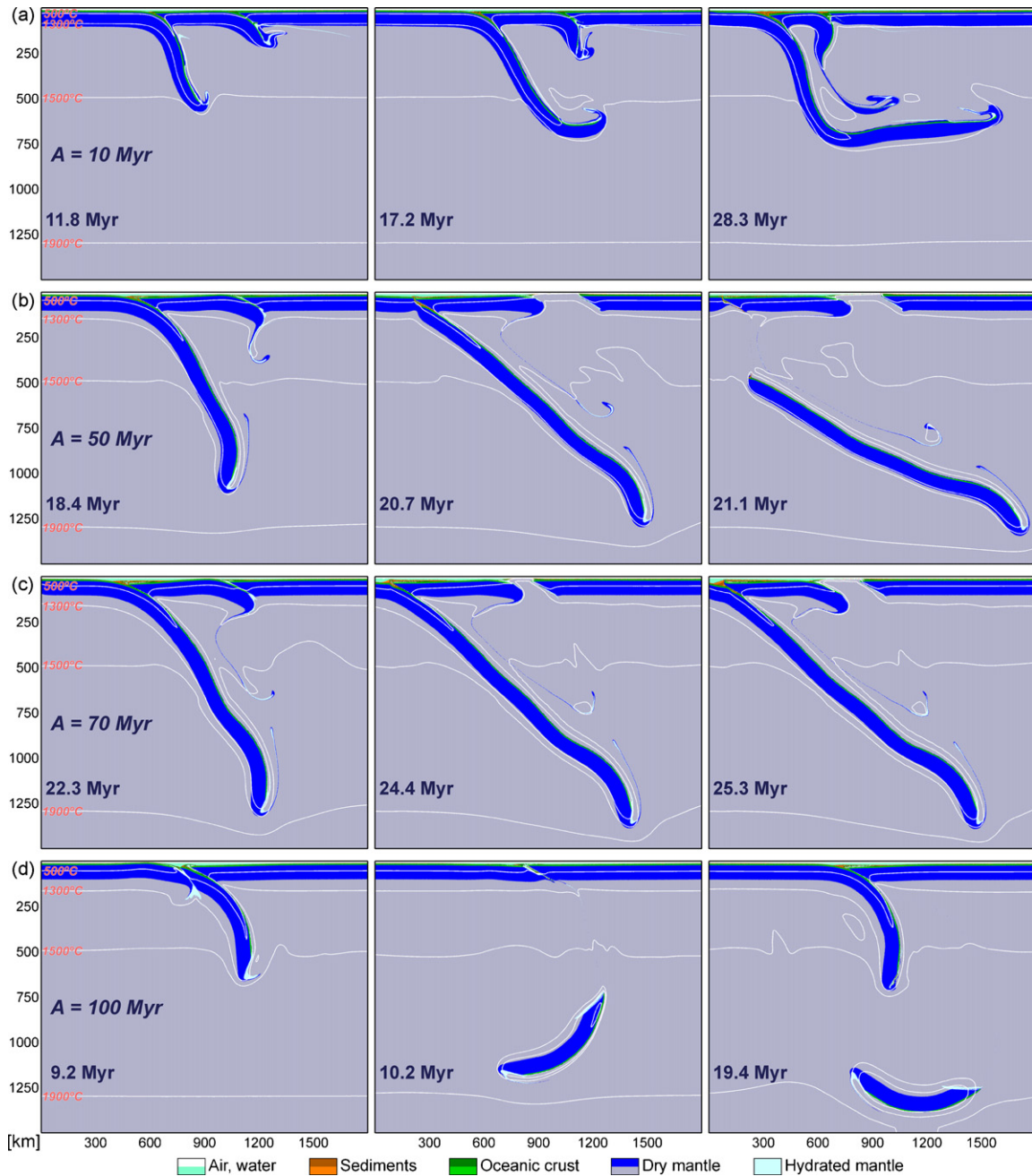


Fig. 11. Influence of age of the lithosphere on the dynamics of double subduction. (a) Model 13, (b) Model 14, (c) Model 15 and (d) Model 16 (model descriptions in Table 3).

dynamics creating further possibilities for forming of gravitationally unstable plate boundaries.

Subduction flip of the middle plate is another specific phenomenon in numerical experiments of double subduction (Fig. 14). The role of a second subduction seems important in triggering this process, which is worth discussing as it can shed light on the open question of subduction initiation mechanisms (e.g. Bercovici, 2003). Subduction flip occurs in experiments where subduction cessation or eduction of the second zone is associated with shallow breakoff of the left plate. The detached sinking slab hence initiates subduction of the middle plate in the direction opposite to the original one (Models 6 and 7 in Table 3; Fig. 9a and b; Fig. 14 is zoom to Fig. 9b), and in some conditions the middle plate can be even flipped because of slabs coupling (Fig. 14, 25 Myr).

Slab breakoff (e.g. Gerya et al., 2004b; Wortel and Spakman, 2000) may be a precursor to subduction initiation of the middle plate.

4.3. Slab interaction with the 660 km discontinuity

The petrological model we employed includes deep mantle phase transitions and thus allows studying possible interactions between slabs and mantle discontinuities and to compare numerical results with seismic tomography of deep structure of the Earth. Seismic structures for two typical scenarios of slab interaction with the discontinuity at 660 km in the studied system are shown in Fig. 16. Seismic velocities were computed on the basis of Gibbs energy minimization approach using

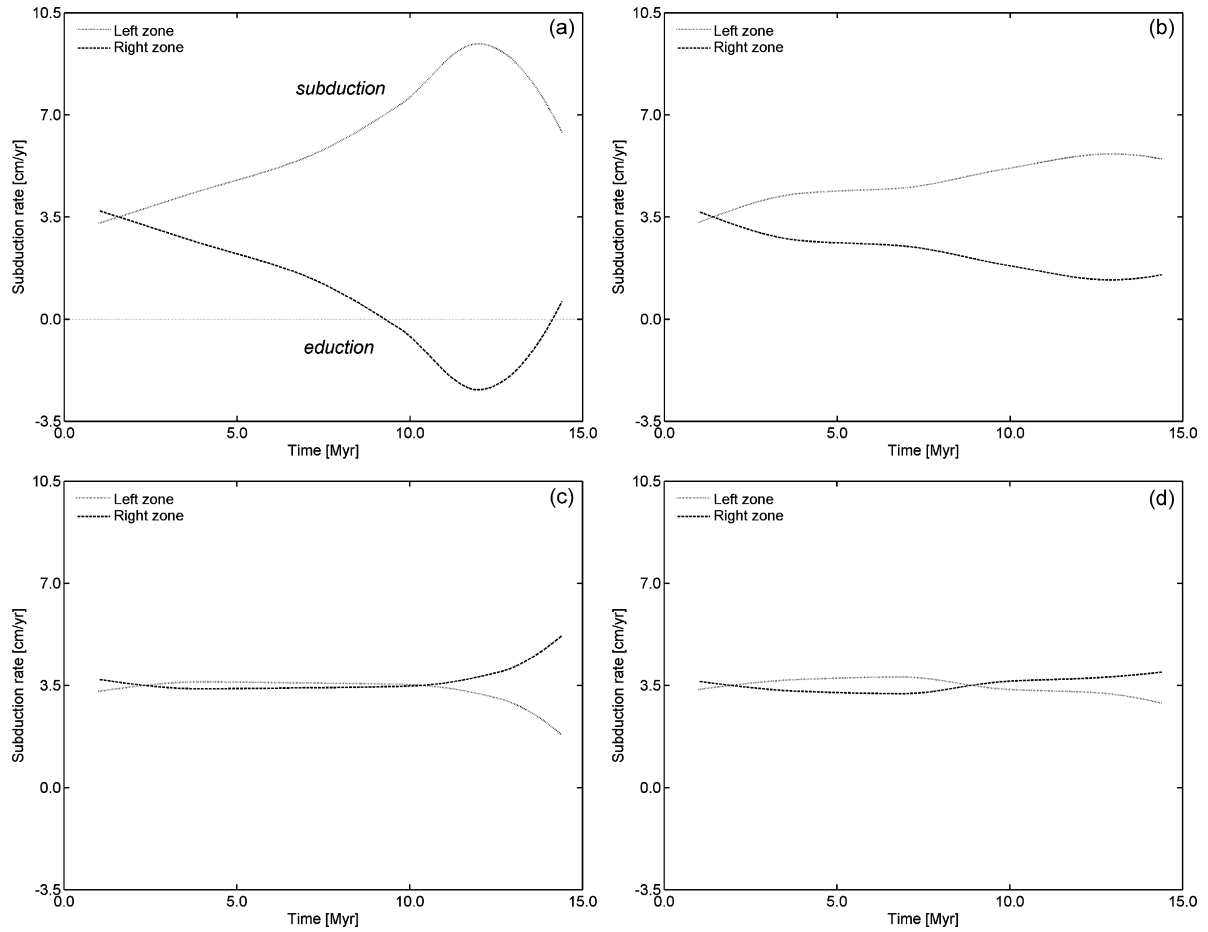


Fig. 12. Subduction rates along first and second subduction zones as functions of time. (a) Model 6, Fig. 9a, (b) Model 11, Fig. 10b, (c) Model 8, Fig. 9c and (d) Model 9, Fig. 9d (model descriptions in Table 3).

methods described by Connolly and Kerrick (2002) and Gerya et al. (2006), and velocities anomalies were calculated compared to the profile with no lithosphere at the top ($A=1$ yr, Fig. 15).

Examples of slabs not penetrating the 660 km discontinuity are shown in Fig. 16a and b and correspond, respectively to Model 3 at 11.0 Myr (see also Fig. 8b) and Model 4 at 6.6 Myr (see also Fig. 8c). Thus, at some range of model conditions (e.g. young slabs, Fig. 11a,

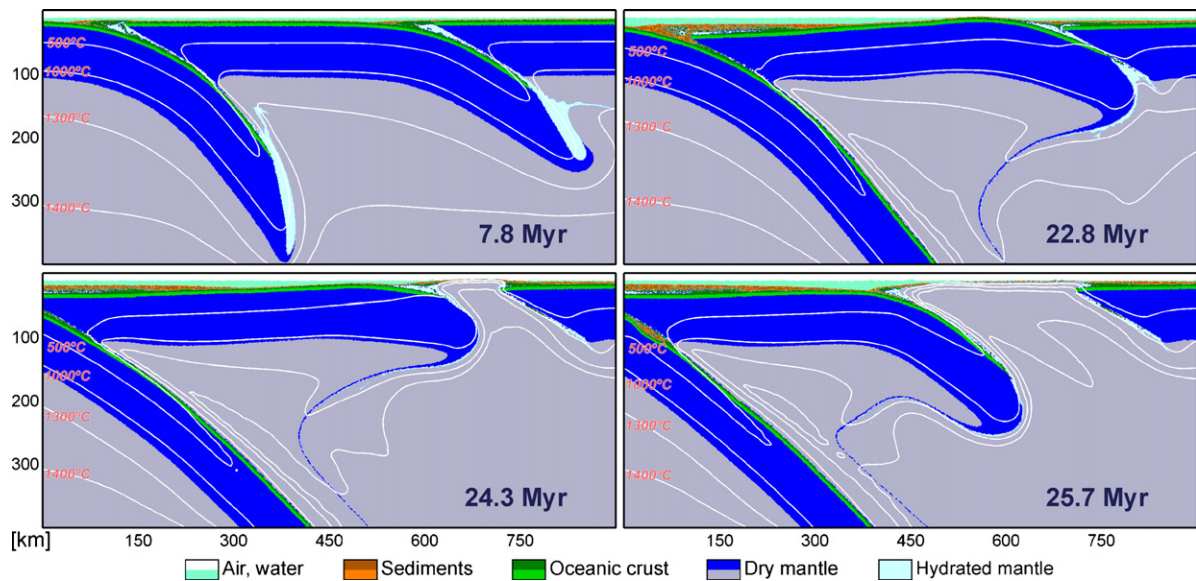


Fig. 13. Eduction of the middle plate (zoom to Fig. 11c; Model 15 in Table 3). Note that subduction of the middle plate is re-initiated at a late stage.

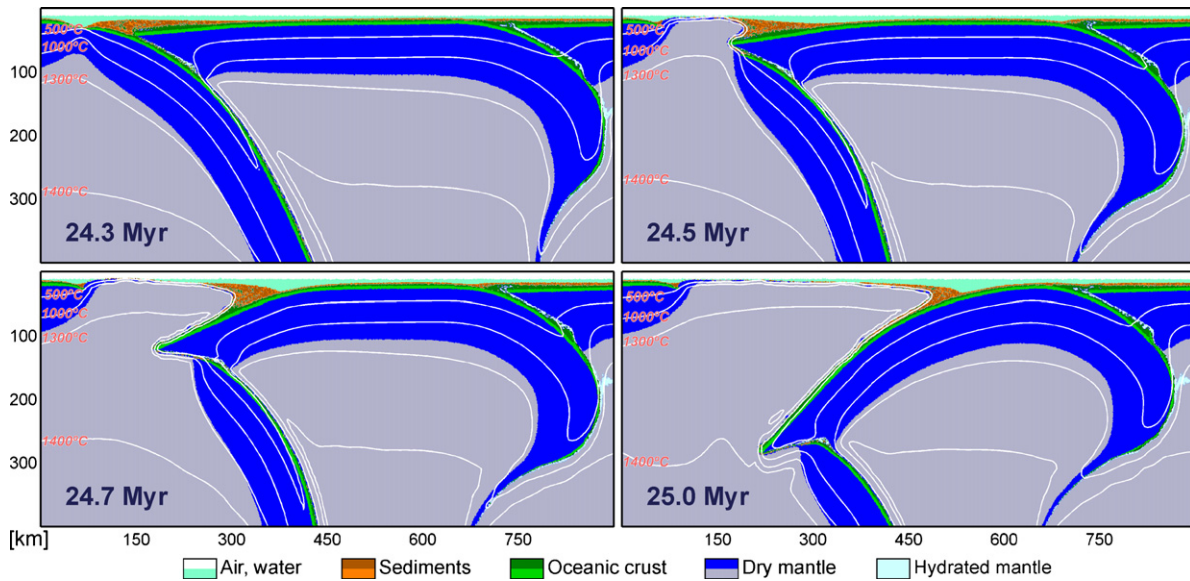


Fig. 14. Triggering of inverse subduction of the middle plate by slab detached from the right plate at shallow depth (zoom to Fig. 9b; Model 7 in Table 3).

slow convergence, Fig. 8a, dominating overriding plate movement, Fig. 8b, middle plate up-side-down flip, Fig. 8c) subducted slabs can be deferred by the discontinuity and flatten at it. Seismic tomography data provide evidence that such a process can occur in many places, for example subducted slabs beneath Izu-Bonin (Fig. 17, from Widiyantoro et al., 1999).

On the other hand both attached and detached slabs can penetrate the 660 km discontinuity. Seismic structures fitting such

examples are shown on Fig. 16c and d (correspond, respectively to Model 14 in Table 3 at 20.7 and 21.1 Myr; see also Fig. 11b). In such a scenario, slab sinks down rapidly with penetration of the discontinuity, normally breaking off at shallow depths. Seismic tomography studies of deep structure of the Earth show that such type of interaction with 660 km discontinuity also can take place, for example Farallon slab beneath North and Central America (Fig. 18, from van der Hilst et al., 1997).

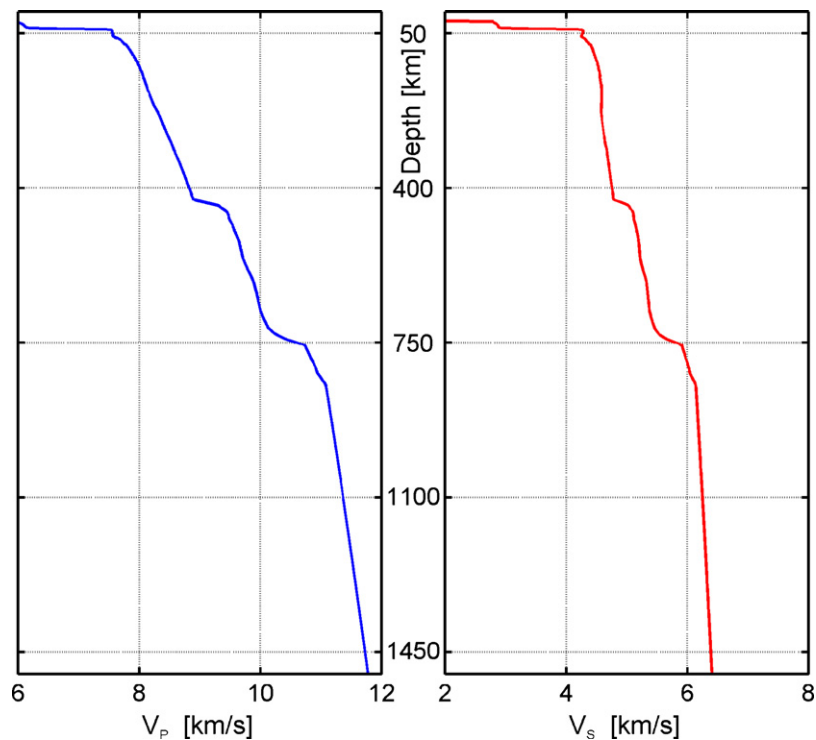


Fig. 15. Standard seismic velocities profile used for calculation of seismic anomalies in Fig. 16.

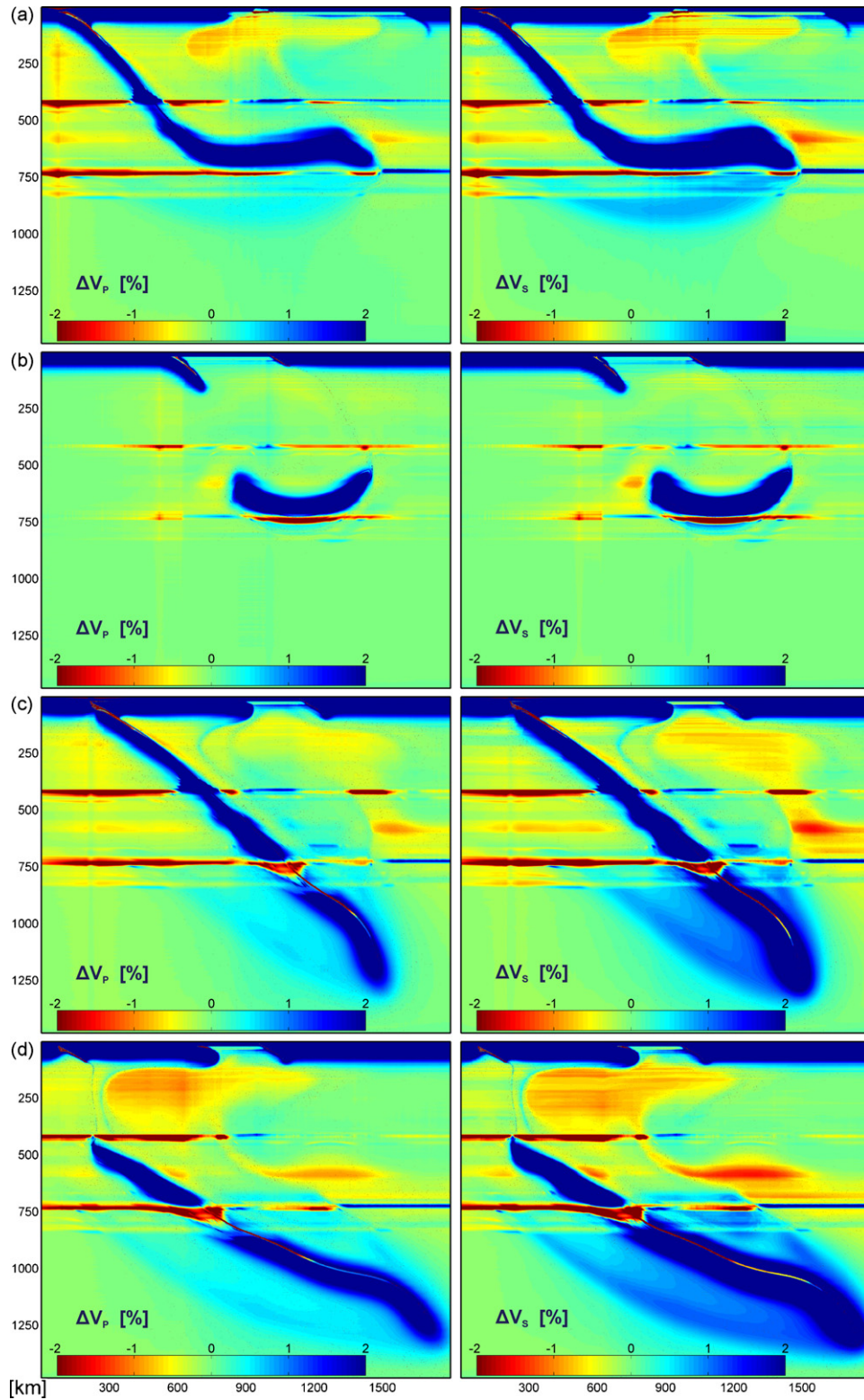


Fig. 16. Seismic structures. (a) Model 3, Fig. 8b, 11.0 Myr, (b) Model 4, Fig. 8c, 6.6 Myr, (c) Model 14, Fig. 11b, 20.7 Myr and (d) Model 14, Fig. 11b, 21.1 Myr (model descriptions in Table 3).

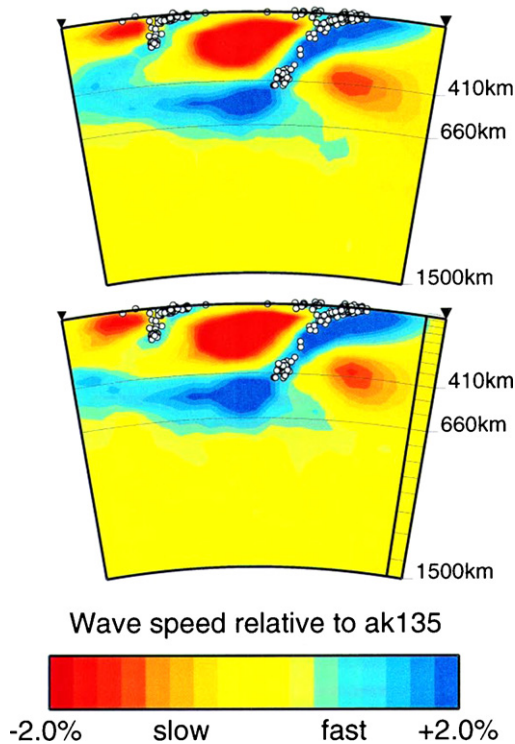


Fig. 17. Vertical cross-section of tomographic image across Ryukyu and Izu-Bonin. Top: recovered from P-wave data and bottom: recovered from S-wave data (from Widiyantoro et al., 1999).

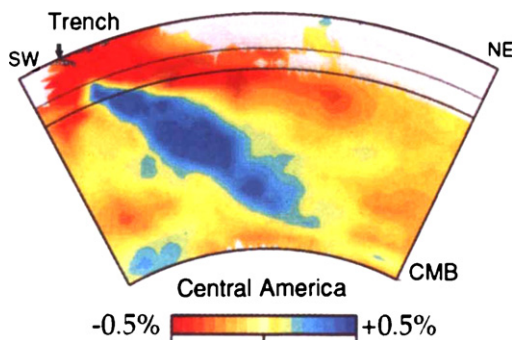


Fig. 18. Vertical cross-section of tomographic image across the convergent margin in Central America. Recovered from P-wave data (from van der Hilst et al., 1997).

5. Conclusions

2D numerical modeling of double subduction leads to the following conclusions:

1. Subduction rates at two parallel zones vary in time even when the total convergence rate remains constant. Dominance of either zone depends on (i) relative rates of the converging plates, (ii) slab ages and (iii) length of the middle plate.
2. Dynamics of double subductions involve specific processes such as (i) eduction, (ii) subduction re-initiation, (iii) subduction flip and (iv) turn-over of detached slabs.
3. Simulated tomographic structures related to slab propagation account for both penetration and non-penetration of the 660 km discontinuity. Non-penetration is favored by (i) low convergence rate, (ii) faster relative movement of the overriding plate, (iii) young ages of subducting slab and (iv) turn-over of the detached slab.

Acknowledgments

This work was supported by ETH Research Grants 0-20437-07, TH-12/05-3, by SNF Research Grant 200021-113672/1. Constructive reviews by two anonymous reviewers are appreciated.

References

- Andersen, T.B., Jamtveit, B., Dewey, J.F., Swensson, E., 1991. Subduction and eduction of continental crust: major mechanisms during continent–continent collision and orogenic extensional collapse, a model based on the south Norwegian Caledonides. *Terra Nova* 3, 303–310.
- Andrews, E.R., Billen, M.L., in press. Rheologic controls on the dynamics of slab detachment. *Tectonophysics*. doi:10.1016/j.tecto.2007.09.004.
- Bercovici, D., 2003. The generation of plate tectonics from mantle convection. *Earth Planet Sci. Lett.* 205, 107–121.
- Boutelier, D., Chemenda, A., Burg, J.-P., 2003. Subduction versus accretion of intra-oceanic volcanic arcs: insight from thermo-mechanical analogue experiments. *Earth Planet Sci. Lett.* 212, 31–45.
- Burg, J.-P., 2006. Two orogenic systems and a transform-transfer Fault in the Himalayas: evidence and consequences. *Earth Sci. Front.* 13, 27–46.
- Burg, J.-P., Jagoutz, O., Dawood, H., Hussain, S.S., 2006. Precollision tilt of crustal blocks in rifted island arcs: structural evidence from the Kohistan Arc. *Tectonics* 25, TC5005.
- Clauser, C., Huenges, E., 1995. Thermal conductivity of rocks and minerals. In: Ahrens, T.J. (Ed.), *Rock Physics and Phase Relations*. American Geophysical Union, Washington, DC, pp. 105–126.
- Connolly, J.A.D., 2005. Computation of phase equilibria by linear programming: a tool for geodynamic modeling and an application to subduction zone decarbonation. *Earth Planet Sci. Lett.* 236, 524–541.
- Connolly, J.A.D., Kerrick, D.M., 2002. Metamorphic controls on seismic velocity of subducted oceanic crust at 100–250 km depth. *Earth Planet Sci. Lett.* 204, 61–74.
- Dogliani, C., Carminati, E., Cuffaro, M., Scrocca, D., 2007. Subduction kinematics and dynamic constraints. *Earth Sci. Rev.* 83, 125–175.
- Fowler, C.M.R., 2005. *The Solid Earth*. Cambridge University Press, Cambridge, p. 685.
- Gerya, T.V., Yuen, D.A., 2003a. Characteristics-based marker-in-cell method with conservative finite-differences schemes for modelling geological flows with strongly variable transport properties. *Phys. Earth Planet Interiors* 140, 295–320.
- Gerya, T.V., Yuen, D.A., 2003b. Rayleigh–Taylor instabilities from hydration and melting propel cold plumes at subduction zones. *Earth Planet Sci. Lett.* 212, 47–62.
- Gerya, T.V., Perchuk, L.L., Maresch, W.V., Willner, A.P., 2004a. Inherent gravitational instability of hot continental crust: implication for doming and diapirism in granulite facies terrains. In: Whitney, D., Teyssier, C., Siddoway, C.S. (Eds.), *Gneiss Domes in Orogeny*. GSA Special Paper, pp. 117–127.
- Gerya, T.V., Yuen, D.A., Maresch, W.V., 2004b. Thermomechanical modelling of slab detachment. *Earth Planet Sci. Lett.* 226, 101–116.
- Gerya, T.V., Connolly, J.A.D., Yuen, D.A., Górczyk, W., Capel, A.M., 2006. Seismic implications of mantle wedge plumes. *Phys. Earth Planet Interiors* 156, 59–74.
- Gerya, T.V., Connolly, J.A.D., Yuen, D.A., 2008. Why is terrestrial subduction one-sided? *Geology* 36, 43–46.
- Hall, R., 1997. Cenozoic plate tectonic reconstructions of SE Asia. *Geol. Soc. Lond. Spec. Pub.* 126, 11–23.
- Hall, R., Ali, J.R., Anderson, C.D., Baker, S.J., 1995. Origin and motion history of the Philippine Sea Plate. *Tectonophysics* 251, 229–250.
- Hall, C.E., Gurnis, M., Sdrolias, M., Lavier, L.L., Muller, R.D., 2003. Catastrophic initiation of subduction following forced convergence across fracture zones. *Earth Planet Sci. Lett.* 212, 15–30.
- Hirose, K., Fei, Y.W., 2002. Subsolidus and melting phase relations of basaltic composition in the uppermost lower mantle. *Geochim. Cosmochim. Acta* 66, 2099–2108.
- Irfune, T., Ringwood, A.E., 1993. Phase transformations in subducted oceanic crust and buoyancy relationships at depths of 600–800 km in the mantle. *Earth Planet Sci. Lett.* 117, 101–110.
- Irfune, T., Ringwood, A.E., Hibberson, W.O., 1994. Subduction of continental crust and terrigenous and pelagic sediments: an experimental study. *Earth Planet Sci. Lett.* 126, 351–368.
- Ishida, M., 1992. Geometry and relative motion of the Philippine Sea plate and Pacific plate beneath the Kanto-Tokai district, Japan. *J. Geophys. Res.* 97, 489–513.
- Khan, A., Connolly, J.A.D., Olsen, N., 2006. Constraining the composition and thermal state of the mantle beneath Europe from inversion of long-period electromagnetic sounding data. *J. Geophys. Res.* 111, B10102.
- King, S.D., 2001. Subduction zones: observations and geodynamic models. *Phys. Earth Planet Interiors* 127, 9–24.
- Manea, V., Gurnis, M., 2007. Subduction zone evolution and low viscosity wedges and channels. *Earth Planet Sci. Lett.* 264, 22–45.
- Maresch, W.V., Gerya, T.V., 2005. Blueschists and blue amphiboles: how much subduction do they need? *Int. Geol. Rev.* 47, 688–702.
- Ono, S., Ohishi, Y., Isshiki, M., Watanuki, T., 2005. In situ X-ray observations of phase assemblages in peridotite and basalt compositions at lower mantle conditions: implications for density of subducted oceanic plate. *J. Geophys. Res.* 110, B02208.

- Ranalli, G., 1995. *Rheology of the Earth*. Chapman and Hall, London, p. 413.
- Regenauer-Lieb, K., Yuen, D.A., Branlund, J., 2001. The initiation of subduction: criticality by addition of water? *Science* 294, 578–580.
- Roth, E.G., Wiens, D.A., 1999. Depression of the 660 km discontinuity beneath the Tonga slab determined from near-vertical ScS reverberations. *Geophys. Res. Lett.* 26, 1223–1226.
- Sobolev, S.V., Babeyko, A.Y., 2005. What drives orogeny in the Andes? *Geology* 33, 617–620.
- Stixrude, L., Bukowinski, M.S.T., 1990. Fundamental thermodynamic relations and silicate melting with implications for the constitution of D'' . *J. Geophys. Res.* 95, 19311–19325.
- Stixrude, L., Lithgow-Bertelloni, C., 2005. Mineralogy and elasticity of the oceanic upper mantle: origin of the low-velocity zone. *J. Geophys. Res.* 110, B03204.
- Tackley, P.J., 2000. Self-consistent generation of tectonic plates in time-dependent, three-dimensional mantle convection simulations. 1. Pseudoplastic yielding. *Geochem. Geophys. Geosyst.* 1, 2000GC000036.
- Tajima, F., Grand, S.P., 1998. Variation of transition zone high-velocity anomalies and depression of the 660 km discontinuity associated with subduction zones from the southern Kuriles to Izu-Bonin and Ryukyu. *J. Geophys. Res.* 103, 15015–15036.
- Takenaka, S., Sanshadokoro, H., Yoshioka, S., 1999. Velocity anomalies and spatial distribution of physical properties in horizontally lying slabs beneath the Northwestern Pacific region. *Phys. Earth Planet Interiors* 112, 137–157.
- Teng, L.S., Lee, C.T., Tsai, Y.B., Hsiao, L.-Y., 2000. Slab breakoff as a mechanism for flipping of subduction polarity in Taiwan. *Geology* 28, 155–158.
- Tibi, R., Wiens, D.A., Shiobara, H., Sugioka, H., Shore, P.J., 2006. Depth of the 660-km discontinuity near the Mariana slab from an array of ocean bottom seismographs. *Geophys. Res. Lett.* 33, L02313.
- Treloar, P.J., Petterson, M.G., Jan, M.Q., Sullivan, M.A., 1996. A re-evaluation of the stratigraphy and evolution of the Kohistan arc sequence, Pakistan Himalaya: implications for magmatic and tectonic arc-building processes. *J. Geol. Soc. Lond.* 153, 681–693.
- Turcotte, D.L., Schubert, G., 2002. *Geodynamics*. Cambridge University Press, Cambridge, p. 456.
- van der Hilst, R.D., Widiyantoro, S., Engdahl, E.R., 1997. Evidence for deep mantle circulation from global tomography. *Nature* 386, 578–584.
- van Hunen, J., van den Berg, A.P., Vlaar, N.J., 2000. A thermomechanical model of horizontal subduction below an overriding plate. *Earth Planet Sci. Lett.* 182, 157–169.
- Widiyantoro, S., Kennett, B.L.N., van der Hilst, R.D., 1999. Seismic tomography with P and S data reveals lateral variations in the rigidity of deep slabs. *Earth Planet Sci. Lett.* 173, 91–100.
- Wortel, M.J.R., Spakman, W., 2000. Geophysics—subduction and slab detachment in the Mediterranean-Carpathian region. *Science* 290, 1910–1917.
- Wu, F., Okaya, D., Sato, H., Hirata, N., 2007. Interaction between two subducting plates under Tokyo and its possible effects on seismic hazards. *Geophys. Res. Lett.* 34, L18301.